28. COSMIC MICROWAVE BACKGROUND

Revised September 2015 by D. Scott (University of British Columbia) and G.F. Smoot (UCB/LBNL).

28.1. Introduction

The energy content in radiation from beyond our Galaxy is dominated by the cosmic microwave background (CMB), discovered in 1965 [1]. The spectrum of the CMB is well described by a blackbody function with $T = 2.7255\,\mathrm{K}$. This spectral form is a main supporting pillar of the hot Big Bang model for the Universe. The lack of any observed deviations from a blackbody spectrum constrains physical processes over cosmic history at redshifts $z \lesssim 10^7$ (see earlier versions of this review).

Currently the key CMB observable is the angular variation in temperature (or intensity) correlations, and now to some extent polarization [2]. Since the first detection of these anisotropies by the Cosmic Background Explorer (*COBE*) satellite [3], there has been intense activity to map the sky at increasing levels of sensitivity and angular resolution by ground-based and balloon-borne measurements. These were joined in 2003 by the first results from NASA's Wilkinson Microwave Anisotropy Probe (*WMAP*) [4], which were improved upon by analyses of the 3-year, 5-year, 7-year, and 9-year *WMAP* data [5,6,7,8]. In 2013 we had the first results [9] from the third generation CMB satellite, ESA's *Planck* mission [10,11], now enhanced by results from the the 2015 *Planck* data release [12,13]. Additionally, CMB anisotropies have been extended to smaller angular scales by ground-based experiments, particularly the Atacama Cosmology Telescope (ACT) [14] and the South Pole Telescope (SPT) [15]. Together these observations have led to a stunning confirmation of the 'Standard Model of Cosmology.' In combination with other astrophysical data, the CMB anisotropy measurements place quite precise constraints on a number of cosmological parameters, and have launched us into an era of precision cosmology. As the CMB turns 50 and the program to map temperature anisotropies is wrapping up, attention is increasingly focussing on polarization measurements as the future arena in which to test fundamental physics.

28.2. CMB Spectrum

It is well known that the spectrum of the microwave background is very precisely that of blackbody radiation, whose temperature evolves with redshift as $T(z) = T_0(1 + z)$ in an expanding universe. As a direct test of its cosmological origin, this relationship is being tested by measuring the strengths of emission and absorption lines in high-redshift systems [16].

Measurements of the spectrum are consistent with a blackbody distribution over more than three decades in frequency (there is a claim by ARCADE [17] of a possible unexpected extragalactic emission signal at low frequency, but the interpretation is debated [18]). All viable cosmological models predict a very nearly Planckian spectrum to within the current observational limits. Because of this, measurements of deviations from a blackbody spectrum have received little attention in recent years, with only a few exceptions. However, that situation may be about to change, since proposed experiments

(such as PIXIE [19]) have the potential to dramatically improve the constraints on energy release in the early Universe. It now seems feasible to probe spectral distortion mechanisms that are *required* in the standard picture, such as those arising from the damping and dissipation of relatively small primordial perturbations, or the average effect of inverse Compton scattering. A more ambitious goal would be to reach the precision needed to detect the residual lines from the cosmological recombination of hydrogen and helium and hence test whether conditions at $z \gtrsim 1000$ accurately follow those in the standard picture [20].

28.3. Description of CMB Anisotropies

Observations show that the CMB contains temperature anisotropies at the 10^{-5} level and polarization anisotropies at the 10^{-6} (and lower) level, over a wide range of angular scales. These anisotropies are usually expressed by using a spherical harmonic expansion of the CMB sky:

$$T(\theta, \phi) = \sum_{\ell m} a_{\ell m} Y_{\ell m}(\theta, \phi)$$

(with the linear polarization pattern written in a similar way using the so-called spin-2 spherical harmonics). Increasing angular resolution requires that the expansion goes to higher and higher multipoles. Because there are only very weak phase correlations seen in the CMB sky and since we notice no preferred direction, the vast majority of the cosmological information is contained in the temperature 2-point function, *i.e.*, the variance as a function only of angular separation. Equivalently, the power per unit $\ln \ell$ is $\ell \sum_m |a_{\ell m}|^2 / 4\pi$.

28.3.1. *The Monopole* :

The CMB has a mean temperature of $T_\gamma = 2.7255 \pm 0.0006\,\mathrm{K}$ (1σ) [21], which can be considered as the monopole component of CMB maps, a_{00}. Since all mapping experiments involve difference measurements, they are insensitive to this average level; monopole measurements can only be made with absolute temperature devices, such as the FIRAS instrument on the *COBE* satellite [22]. The measured kT_γ is equivalent to $0.234\,\mathrm{meV}$ or $4.60 \times 10^{-10}\, m_\mathrm{e} c^2$. A blackbody of the measured temperature has a number density $n_\gamma = (2\zeta(3)/\pi^2)\, T_\gamma^3 \simeq 411\,\mathrm{cm}^{-3}$, energy density $\rho_\gamma = (\pi^2/15)\, T_\gamma^4 \simeq 4.64 \times 10^{-34}\,\mathrm{g\,cm}^{-3} \simeq 0.260\,\mathrm{eV\,cm}^{-3}$, and a fraction of the critical density $\Omega_\gamma \simeq 5.38 \times 10^{-5}$.

28.3.2. *The Dipole* :

The largest anisotropy is in the $\ell = 1$ (dipole) first spherical harmonic, with amplitude $3.3645 \pm 0.0020\,\mathrm{mK}$ [12]. The dipole is interpreted to be the result of the Doppler boosting of the monopole caused by the solar system motion relative to the nearly isotropic blackbody field, as broadly confirmed by measurements of the radial velocities of local galaxies (*e.g.*, Ref. [23]). The motion of an observer with velocity $\beta \equiv v/c$ relative to an isotropic Planckian radiation field of temperature T_0 produces a Lorentz-boosted temperature pattern

$$T(\theta) = T_0 (1 - \beta^2)^{1/2} / (1 - \beta \cos\theta)$$

$$\simeq T_0 \left[1 + \beta\cos\theta + \left(\beta^2/2\right)\cos 2\theta + \mathrm{O}\left(\beta^3\right)\right].$$

At every point in the sky, one observes a blackbody spectrum, with temperature $T(\theta)$. The spectrum of the dipole has been confirmed to be the differential of a blackbody spectrum [24]. At higher order there are additional effects arising from aberration and from modulation of the anisotropy pattern, which have also been observed [25].

The implied velocity for the solar system barycenter is $v = 370.09 \pm 0.22\,\mathrm{km\,s^{-1}}$, assuming a value $T_0 = T_\gamma$, towards $(l, b) = (264.00^\circ \pm 0.03^\circ, 48.24^\circ \pm 0.02^\circ)$ [12]. Such a solar system motion implies a velocity for the Galaxy and the Local Group of galaxies relative to the CMB. The derived value is $v_{\mathrm{LG}} = 627 \pm 22\,\mathrm{km\,s^{-1}}$ towards $(l, b) = (276^\circ \pm 3^\circ, 30^\circ \pm 3^\circ)$ [26], where most of the error comes from uncertainty in the velocity of the solar system relative to the Local Group.

The dipole is a frame-dependent quantity, and one can thus determine the 'absolute rest frame' as that in which the CMB dipole would be zero. Our velocity relative to the Local Group, as well as the velocity of the Earth around the Sun, and any velocity of the receiver relative to the Earth, is normally removed for the purposes of CMB anisotropy study. The dipole is now routinely used as a primary calibrator for mapping experiments, either via the time-varying orbital motion of the Earth, or through the cosmological dipole measured by satellite experiments.

28.3.3. *Higher-Order Multipoles* :

The variations in the CMB temperature maps at higher multipoles ($\ell \geq 2$) are interpreted as being mostly the result of perturbations in the density of the early Universe, manifesting themselves at the epoch of the last scattering of the CMB photons. In the hot Big Bang picture, the expansion of the Universe cools the plasma so that by a redshift $z \simeq 1100$ (with little dependence on the details of the model), the hydrogen and helium nuclei can bind electrons into neutral atoms, a process usually referred to as recombination [27]. Before this epoch, the CMB photons were tightly coupled to the baryons, while afterwards they could freely stream towards us. By measuring the $a_{\ell m}$s we are thus learning directly about physical conditions in the early Universe.

A statistically isotropic sky means that all ms are equivalent, *i.e.*, there is no preferred axis, so that the temperature correlation function between two positions on the sky depends only on angular separation and not orientation. Together with the assumption of Gaussian statistics (*i.e.*, no correlations between the modes), the variance of the temperature field (or equivalently the power spectrum in ℓ) then fully characterizes the anisotropies. The power summed over all ms at each ℓ is $(2\ell + 1)C_\ell/(4\pi)$, where $C_\ell \equiv \left\langle |a_{\ell m}|^2 \right\rangle$. Thus averages of $a_{\ell m}$s over m can be used as estimators of the C_ℓs to constrain their expectation values, which are the quantities predicted by a theoretical model. For an idealized full-sky observation, the variance of each measured C_ℓ (*i.e.*, the variance of the variance) is $[2/(2\ell + 1)]C_\ell^2$. This sampling uncertainty (known as 'cosmic variance') comes about because each C_ℓ is χ^2 distributed with $(2\ell + 1)$ degrees of freedom for our observable volume of the Universe. For fractional sky coverage, f_{sky}, this variance is increased by $1/f_{\mathrm{sky}}$ and the modes become partially correlated.

It is important to understand that theories predict the expectation value of the power spectrum, whereas our sky is a single realization. Hence the cosmic variance is an

unavoidable source of uncertainty when constraining models; it dominates the scatter at lower ℓs, while the effects of instrumental noise and resolution dominate at higher ℓs [28].

Theoretical models generally predict that the $a_{\ell m}$ modes are Gaussian random fields to high precision, matching the empirical tests, *e.g.*, standard slow-roll inflation's non-Gaussian contribution is expected to be at least an order of magnitude below current observational limits [29]. Although non-Gaussianity of various forms is possible in early Universe models, tests show that Gaussianity is an extremely good simplifying approximation [30]. The only current indications of any non-Gaussianity or statistical anisotropy are some relatively weak signatures at large scales, seen in both *WMAP* [31] and *Planck* data [32], but not of high enough significance to reject the simplifying assumption. Nevertheless, models that deviate from the inflationary slow-roll conditions can have measurable non-Gaussian signatures. So while the current observational limits make the power spectrum the dominant probe of cosmology, it is worth noting that higher-order correlations are beginning to be a tool for constraining otherwise viable theories.

28.3.4. *Angular Resolution and Binning* :

There is no one-to-one conversion between multipole ℓ and the angle subtended by a particular spatial scale projected onto the sky. However, a single spherical harmonic $Y_{\ell m}$ corresponds to angular variations of $\theta \sim \pi/\ell$. CMB maps contain anisotropy information from the size of the map (or in practice some fraction of that size) down to the beam-size of the instrument, σ (the standard deviation of the beam, in radians). One can think of the effect of a Gaussian beam as rolling off the power spectrum with the function $\mathrm{e}^{-\ell(\ell+1)\sigma^2}$.

For less than full sky coverage, the ℓ modes become correlated. Hence, experimental results are usually quoted as a series of 'band powers,' defined as estimators of $\ell(\ell+1)C_\ell/2\pi$ over different ranges of ℓ. Because of the strong foreground signals in the Galactic Plane, even 'all-sky' surveys, such as *WMAP* and *Planck* involve a cut sky. The amount of binning required to obtain uncorrelated estimates of power also depends on the map size.

28.4. Cosmological Parameters

The current 'Standard Model' of cosmology contains around 10 free parameters (see The Cosmological Parameters—Sec. 25 of this *Review*). The basic framework is the Friedmann-Robertson-Walker (FRW) metric (*i.e.*, a universe that is approximately homogeneous and isotropic on large scales), with density perturbations laid down at early times and evolving into today's structures (see Big-Bang cosmology—Sec. 22 of this *Review*). The most general possible set of density variations is a linear combination of an adiabatic density perturbation and some isocurvature perturbations. Adiabatic means that there is no change to the entropy per particle for each species, *i.e.*, $\delta\rho/\rho$ for matter is $(3/4)\delta\rho/\rho$ for radiation. Isocurvature means that the set of individual density perturbations adds to zero, for example, matter perturbations compensate radiation perturbations so that the total energy density remains unperturbed, *i.e.*, $\delta\rho$ for matter is $-\delta\rho$ for radiation. These different modes give rise to distinct (temporal) phases during growth, with those of the adiabatic scenario looking exactly like the data. Models

that generate mainly isocurvature type perturbations (such as most topological defect scenarios) are no longer considered to be viable. However, an admixture of the adiabatic mode with up to about 4% isocurvature contribution (depending on details of the mode) is still allowed [33,34].

28.4.1. ***Initial Condition Parameters*** :

Within the adiabatic family of models, there is, in principle, a free function describing the variation of comoving curvature perturbations, $\mathcal{R}(\mathbf{x}, t)$. The great virtue of $\mathcal{R}$ is that it is constant in time for a purely adiabatic perturbation. There are physical reasons to anticipate that the variance of these perturbations will be described well by a power law in scale, *i.e.*, in Fourier space $\left\langle |\mathcal{R}|_k^2 \right\rangle \propto k^{n_\mathrm{s}-4}$, where k is wavenumber and n_s is the usual definition of spectral index. So-called 'scale-invariant' initial conditions (meaning gravitational potential fluctuations that are independent of k) correspond to $n_\mathrm{s} = 1$. In inflationary models [35] (see upcoming review on inflation), perturbations are generated by quantum fluctuations, which are set by the energy scale of inflation, together with the slope and higher derivatives of the inflationary potential. One generally expects that the Taylor series expansion of $\ln \mathcal{R}_k(\ln k)$ has terms of steadily decreasing size. For the simplest models, there are thus two parameters describing the initial conditions for density perturbations, namely the amplitude and slope of the power spectrum. These can be explicitly defined, for example, through:

$$\Delta^2_{\mathcal{R}} \equiv (k^3/2\pi^2) \left\langle |\mathcal{R}|_k^2 \right\rangle \simeq A_\mathrm{s} \, (k/k_0)^{n_\mathrm{s}-1} \,,$$

with $A_\mathrm{s} \equiv \Delta^2_{\mathcal{R}}(k_0)$ and $k_0 = 0.05\,\mathrm{Mpc}^{-1}$, say. There are many other equally valid definitions of the amplitude parameter (see also Secs. 22, 25, and upcoming review on inflation of this *Review*), and we caution that the relationships between some of them can be cosmology-dependent. In 'slow roll' inflationary models, this normalization is proportional to the combination $V^3/(V')^2$, for the inflationary potential $V(\phi)$. The slope n_s also involves V'', and so the combination of A_s and n_s can constrain potentials.

Inflation generates tensor (gravitational wave) modes, as well as scalar (density perturbation) modes. This fact introduces another parameter, measuring the amplitude of a possible tensor component, or equivalently the ratio of the tensor to scalar contributions. The tensor amplitude is $A_\mathrm{t} \propto V$, and thus one expects a larger gravitational wave contribution in models where inflation happens at higher energies. The tensor power spectrum also has a slope, often denoted n_t, but since this seems unlikely to be measured in the near future, it is sufficient for now to focus only on the amplitude of the gravitational wave component. It is most common to define the tensor contribution through r, the ratio of tensor to scalar perturbation spectra at some small value of k (although sometimes it is defined in terms of the ratio of contributions at $\ell = 2$). Different inflationary potentials will lead to different predictions, *e.g.*, for 50 e-folds $\lambda\phi^4$ inflation gives $r = 0.32$ and $m^2\phi^2$ inflation gives $r = 0.16$ (both now disfavored by the data), while other models can have arbitrarily small values of r. In any case, whatever the specific definition, and whether they come from inflation or something else, the 'initial conditions' give rise to a minimum of three parameters, A_s, n_s, and r.

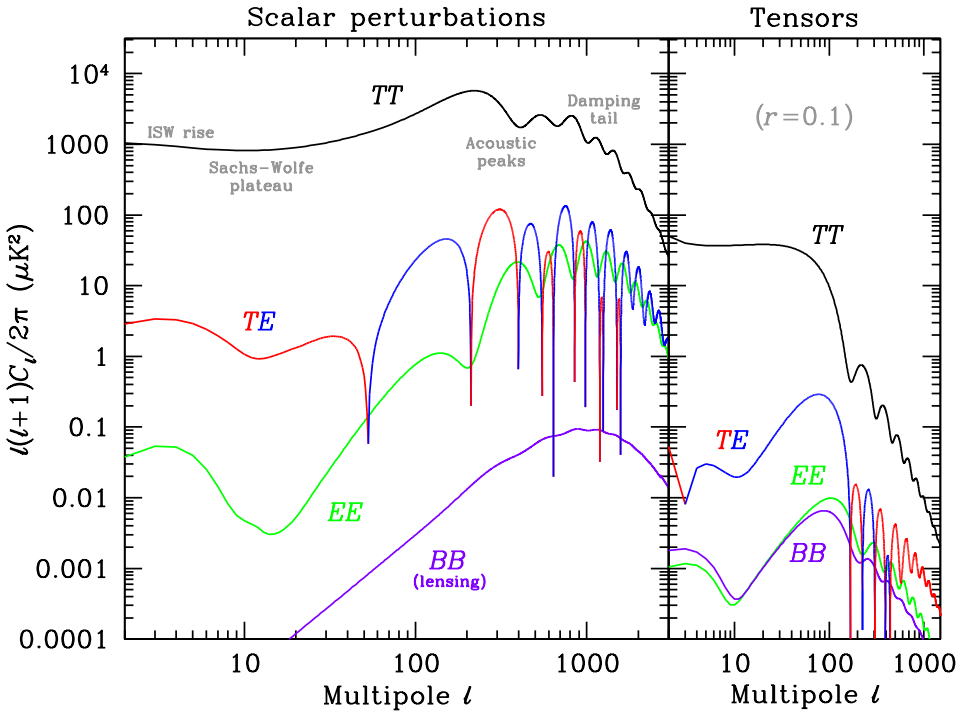

Figure 28.1: Theoretical CMB anisotropy power spectra, using the best-fitting ΛCDM model from *Planck*, calculated using `CAMB`. The panel on the left shows the theoretical expectation for scalar perturbations, while the panel on the right is for tensor perturbations with an amplitude set to $r = 0.1$. Note that the x-axis is logarithmic here. For the well-measured scalar TT spectrum, the regions, each covering roughly a decade in ℓ, are labeled as in the text: the ISW rise; Sachs-Wolfe plateau; acoustic peaks; and damping tail. The TE cross-correlation power spectra change sign, and that has been indicated by plotting the absolute value, but switching color for the negative parts.

28.4.2. *Background Cosmology Parameters* :

The FRW cosmology requires an expansion parameter (the Hubble Constant, H_0, often represented through $H_0 = 100\,h\,\mathrm{km\,s^{-1}Mpc^{-1}}$) and several parameters to describe the matter and energy content of the Universe. These are usually given in terms of the critical density, *i.e.*, for species 'x,' $\Omega_\mathrm{x} \equiv \rho_\mathrm{x}/\rho_\mathrm{crit}$, where $\rho_\mathrm{crit} \equiv 3H_0^2/8\pi G$. Since physical densities $\rho_\mathrm{x} \propto \Omega_\mathrm{x}h^2 \equiv \omega_\mathrm{x}$ are what govern the physics of the CMB anisotropies, it is these ωs that are best constrained by CMB data. In particular CMB, observations constrain $\Omega_\mathrm{b}h^2$ for baryons and $\Omega_\mathrm{c}h^2$ for cold dark matter (with $\rho_\mathrm{m} = \rho_\mathrm{c} + \rho_\mathrm{b}$ for the sum).

The contribution of a cosmological constant Λ (or other form of dark energy, see Dark Energy—Sec. 27) is usually included via a parameter that quantifies the curvature, $\Omega_K \equiv 1 - \Omega_\mathrm{tot}$, where $\Omega_\mathrm{tot} = \Omega_\mathrm{m} + \Omega_\Lambda$. The radiation content, while in principle a free parameter, is precisely enough determined by the measurement of T_γ, and makes a $< 10^{-4}$ contribution to Ω_tot today.

Astrophysical processes at relatively low redshift can also affect the C_ℓs, with a particularly significant effect coming through reionization. The Universe became reionized at some redshift $z_{\rm i}$, long after recombination, affecting the CMB through the integrated Thomson scattering optical depth:

$$\tau = \int_0^{z_{\rm i}} \sigma_{\rm T} n_{\rm e}(z) \frac{dt}{dz} dz,$$

where $\sigma_{\rm T}$ is the Thomson cross-section, $n_{\rm e}(z)$ is the number density of free electrons (which depends on astrophysics), and dt/dz is fixed by the background cosmology. In principle, τ can be determined from the small-scale matter power spectrum, together with the physics of structure formation and radiative feedback processes; however, this is a sufficiently intricate calculation that in practice τ needs to be considered as a free parameter.

Thus, we have eight basic cosmological parameters: $A_{\rm s}$, $n_{\rm s}$, r, h, $\Omega_{\rm b}h^2$, $\Omega_{\rm c}h^2$, $\Omega_{\rm tot}$, and τ. One can add additional parameters to this list, particularly when using the CMB in combination with other data sets. The next most relevant ones might be: $\Omega_\nu h^2$, the massive neutrino contribution; w ($\equiv p/\rho$), the equation of state parameter for the dark energy; and $dn_{\rm s}/d\ln k$, measuring deviations from a constant spectral index. To these 11 one could of course add further parameters describing additional physics, such as details of the reionization process, features in the initial power spectrum, a sub-dominant contribution of isocurvature modes, *etc.*

As well as these underlying parameters, there are other (dependent) quantities that can be obtained from them. Such derived parameters include the actual Ωs of the various components (*e.g.*, $\Omega_{\rm m}$), the variance of density perturbations at particular scales (*e.g.*, σ_8), the angular scale of the sound horizon (θ_*), the age of the Universe today (t_0), the age of the Universe at recombination, reionization, *etc.* (see The Cosmological Parameters—Sec. 25).

28.5. Physics of Anisotropies

The cosmological parameters affect the anisotropies through the well understood physics of the evolution of linear perturbations within a background FRW cosmology. There are very effective, fast, and publicly available software codes for computing the CMB anisotropy, polarization, and matter power spectra, *e.g.*, `CMBFAST` [36] and `CAMB` [37]. These have been tested over a wide range of cosmological parameters and are considered to be accurate to much better than the 1% level [38], so that numerical errors are less than 10% of the parameter uncertainties for *Planck* [9].

For pedagogical purposes, it is easiest to focus on the temperature anisotropies, before moving to the polarization power spectra. A description of the physics underlying the C_ℓ^{TT}s can be separated into four main regions (the first two combined below), as shown in the top left part of Fig. 28.1.

28.5.1. *The ISW Rise,* $\ell \lesssim 10$*, and Sachs-Wolfe Plateau,* $10 \lesssim \ell \lesssim 100$:

The horizon scale (or more precisely, the angle subtended by the Hubble radius) at last scattering corresponds to $\ell \simeq 100$. Anisotropies at larger scales have not evolved significantly, and hence directly reflect the 'initial conditions.' Temperature variations are $\delta T/T = -(1/5)\mathcal{R}(\mathbf{x}_{\rm LSS}) \simeq (1/3)\delta\phi/c^2$, where $\delta\phi$ is the perturbation to the gravitational potential, evaluated on the last scattering surface (LSS). This is a result of the combination of gravitational redshift and intrinsic temperature fluctuations, and is usually referred to as the Sachs-Wolfe effect [39].

Assuming that a nearly scale-invariant spectrum of curvature and corresponding density perturbations was laid down at early times (*i.e.*, $n_{\rm s} \simeq 1$, meaning equal power per decade in k), then $\ell(\ell+1)C_\ell \simeq$ constant at low ℓs. This effect is hard to see unless the multipole axis is plotted logarithmically (as in Fig. 28.1, and part of Fig. 28.2).

Time variation of the potentials (*i.e.*, time-dependent metric perturbations) leads to an upturn in the C_ℓs in the lowest several multipoles; any deviation from a total equation of state $w = 0$ has such an effect. So the dominance of the dark energy at low redshift (see Dark Energy—Sec. 27) makes the lowest ℓs rise above the plateau. This is sometimes called the integrated Sachs-Wolfe effect (or ISW rise), since it comes from the line integral of $\dot{\phi}$; it has been confirmed through correlations between the large-angle anisotropies and large-scale structure [40]. Specific models can also give additional contributions at low ℓ (*e.g.*, perturbations in the dark energy component itself [41]), but typically these are buried in the cosmic variance.

In principle, the mechanism that produces primordial perturbations could generate scalar, vector, and tensor modes. However, the vector (vorticity) modes decay with the expansion of the Universe. The tensors (transverse trace-free perturbations to the metric) generate temperature anisotropies through the integrated effect of the locally anisotropic expansion of space. Since the tensor modes also redshift away after they enter the horizon, they contribute only to angular scales above about 1° (see Fig. 28.1). Hence some fraction of the low-ℓ signal could be due to a gravitational wave contribution, although small amounts of tensors are essentially impossible to discriminate from other effects that might raise the level of the plateau. Nevertheless, the tensors *can* be distinguished using polarization information (see Sec. 28.7).

28.5.2. *The Acoustic Peaks,* $100 \lesssim \ell \lesssim 1000$:

On sub-degree scales, the rich structure in the anisotropy spectrum is the consequence of gravity-driven acoustic oscillations occurring before the atoms in the Universe became neutral. Perturbations inside the horizon at last scattering have been able to evolve causally and produce anisotropy at the last scattering epoch, which reflects this evolution. The frozen-in phases of these sound waves imprint a dependence on the cosmological parameters, which gives CMB anisotropies their great constraining power.

The underlying physics can be understood as follows. Before the Universe became neutral, the proton-electron plasma was tightly coupled to the photons, and these components behaved as a single 'photon-baryon fluid.' Perturbations in the gravitational potential, dominated by the dark matter component, were steadily evolving. They drove oscillations in the photon-baryon fluid, with photon pressure providing most of the restoring force and baryons giving some additional inertia. The perturbations were quite

small in amplitude, $O(10^{-5})$, and so evolved linearly. That means each Fourier mode developed independently, and hence can be described by a driven harmonic oscillator, with frequency determined by the sound speed in the fluid. Thus the fluid density underwent oscillations, giving time variations in temperature. These combine with a velocity effect, which is $\pi/2$ out of phase and has its amplitude reduced by the sound speed.

After the Universe recombined, the radiation decoupled from the baryons and could travel freely towards us. At that point, the (temporal) phases of the oscillations were frozen-in, and became projected on the sky as a harmonic series of peaks. The main peak is the mode that went through 1/4 of a period, reaching maximal compression. The even peaks are maximal *under*-densities, which are generally of smaller amplitude because the rebound has to fight against the baryon inertia. The troughs, which do not extend to zero power, are partially filled by the Doppler effect because they are at the velocity maxima.

The physical length scale associated with the peaks is the sound horizon at last scattering, which can be straightforwardly calculated. This length is projected onto the sky, leading to an angular scale that depends on the geometry of space, as well as the distance to last scattering. Hence the angular position of the peaks is a sensitive probe of a particular combination of cosmological parameters. In fact, the angular scale, θ_*, is the most precisely measured observable, and hence is often treated as an element of the cosmological parameter set.

One additional effect arises from reionization at redshift $z_{\rm i}$. A fraction of photons (τ) will be isotropically scattered at $z < z_{\rm i}$, partially erasing the anisotropies at angular scales smaller than those subtended by the Hubble radius at $z_{\rm i}$. This corresponds typically to ℓs above a few 10s, depending on the specific reionization model. The acoustic peaks are therefore reduced by a factor $e^{-2\tau}$ relative to the plateau.

These peaks were a clear theoretical prediction going back to about 1970 [42]. One can think of them as a snapshot of stochastic standing waves. Since the physics governing them is simple and their structure rich, then one can see how they encode extractable information about the cosmological parameters. Their empirical existence started to become clear around 1994 [43], and the emergence, over the following decade, of a coherent series of acoustic peaks and troughs is a triumph of modern cosmology. This picture has received further confirmation with the detection in the power spectrum of galaxies (at redshifts close to zero) of the imprint of these same acoustic oscillations in the baryon component [44], as well as through detection of the expected oscillations in CMB polarization power spectra (see Sec. 28.7).

28.5.3. *The Damping Tail, $\ell \gtrsim 1000$* :

The recombination process is not instantaneous, which imparts a thickness to the last scattering surface. This leads to a damping of the anisotropies at the highest ℓs, corresponding to scales smaller than that subtended by this thickness. One can also think of the photon-baryon fluid as having imperfect coupling, so that there is diffusion between the two components, and hence the amplitudes of the oscillations decrease with time. These effects lead to a damping of the C_ℓs, sometimes called Silk damping [45], which cuts off the anisotropies at multipoles above about 2000. So, although in principle it is possible to measure to ever smaller scales, this becomes increasingly difficult in practice.

28.5.4. *Gravitational Lensing Effects* :

An extra effect at high ℓs comes from gravitational lensing, caused mainly by non-linear structures at low redshift. The C_ℓs are convolved with a smoothing function in a calculable way, partially flattening the peaks and troughs, generating a power-law tail at the highest multipoles, and complicating the polarization signal [46]. The effects of lensing on the CMB have now been definitively detected through the 4-point function, which correlates temperature gradients and small-scale anisotropies (enabling a map of the lensing potential to be constructed [47,48]), as well as through the smoothing effect on the shape of the C_ℓs. Lensing is important because it gives an independent estimate of $A_{\rm s}$, breaking the parameter combination $A_{\rm s}{\rm e}^{-2\tau}$ that is largely degenerate in the anisotropy power spectra.

Lensing is an example of a 'secondary effect,' *i.e.*, the processing of anisotropies due to relatively nearby structures (see Sec. 28.8.2). Galaxies and clusters of galaxies give several such effects; all are expected to be of low amplitude, but are increasingly important at the highest ℓs. Such effects carry additional cosmological information (about evolving gravitational potentials in the low-redshift Universe) and are increasing in importance as experiments push to higher sensitivity and angular resolution. Measurements of the lensing power spectrum at high ℓ are a particularly sensitive probe of the sum of the neutrino masses [49].

28.6. Current Temperature Anisotropy Data

There has been a steady improvement in the quality of CMB data that has led to the development of the present-day cosmological model. The most robust constraints currently available come from *Planck* satellite [50,51] data combined with smaller scale results from the ACT [52] and SPT [53] experiments (together with constraints from non-CMB cosmological data-sets). We plot power spectrum estimates from these experiments in Fig. 28.2, along with *WMAP* data [8] to show the consistency (see previous versions of this review for data from earlier experiments). Comparisons among data-sets show very good agreement, both in maps and in derived power spectra (up to systematic uncertainties in the overall calibration for some experiments). This makes it clear that systematic effects are largely under control.

The band-powers shown in Fig. 28.2 are in very good agreement with a 'ΛCDM' model. As described earlier, several (at least eight) of the peaks and troughs are quite apparent. For details of how these estimates were arrived at, the strength of correlations between band-powers and other information required to properly interpret them, the original papers should be consulted.

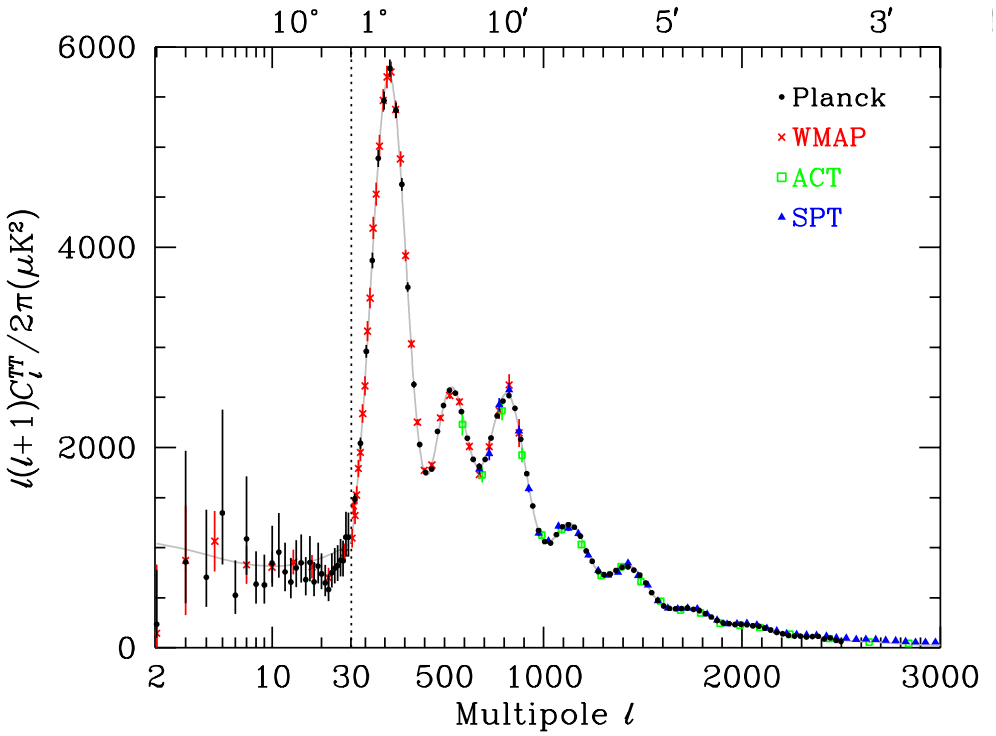

Figure 28.2: CMB temperature anisotropy band-power estimates from the *Planck*, *WMAP*, ACT, and SPT experiments. Note that the widths of the ℓ-bands vary between experiments and have not been plotted. This figure represents only a selection of the most recent available experimental results, and some points with large error bars have been omitted. At the higher multipoles these band-powers involve subtraction of particular foreground models, while proper analysis requires simultaneous fitting of CMB and foregrounds over multiple frequencies. The x-axis here is logarithmic for the lowest multipoles, to show the Sachs-Wolfe plateau, and linear for the other multipoles. The acoustic peaks and damping region are very clearly observed, with no need for a theoretical curve to guide the eye; however, the curve plotted is the best-fit *Planck* model.

28.7. CMB Polarization

Since Thomson scattering of an anisotropic radiation field also generates linear polarization, the CMB is predicted to be polarized at the level of roughly 5% of the temperature anisotropies [54]. Polarization is a spin-2 field on the sky, and the algebra of the modes in ℓ-space is strongly analogous to spin-orbit coupling in quantum mechanics [55]. The linear polarization pattern can be decomposed in a number of ways, with two quantities required for each pixel in a map, often given as the Q and U Stokes parameters. However, the most intuitive and physical decomposition is a geometrical one, splitting the polarization pattern into a part that comes from a divergence (often referred to as the 'E-mode') and a part with a curl (called the 'B-mode') [56]. More explicitly, the modes are defined in terms of second derivatives of the polarization amplitude, with the Hessian for the E-modes having principle axes in the same sense as the polarization,

while the B-mode pattern can be thought of as a 45° rotation of the E-mode pattern. Globally one sees that the E-modes have $(-1)^{\ell}$ parity (like the spherical harmonics), while the B-modes have $(-1)^{\ell+1}$ parity.

The existence of this linear polarization allows for six different cross power spectra to be determined from data that measure the full temperature and polarization anisotropy information. Parity considerations make two of these zero, and we are left with four potential observables, C_ℓ^{TT}, C_ℓ^{TE}, C_ℓ^{EE}, and C_ℓ^{BB} (see Fig. 28.1). Because scalar perturbations have no handedness, the B-mode power spectrum can only be sourced by vectors or tensors. Moreover, since inflationary scalar perturbations give only E-modes, while tensors generate roughly equal amounts of E- and B-modes, then the determination of a non-zero B-mode signal is a way to measure the gravitational wave contribution (and thus potentially derive the energy scale of inflation). However, since the signal is expected to be rather weak, one must first eliminate the foreground contributions and other systematic effects down to very low levels.

The polarization C_ℓs also exhibit a series of acoustic peaks generated by the oscillating photon-baryon fluid. The main 'EE' power spectrum has peaks that are out of phase with those in the 'TT' spectrum, because the polarization anisotropies are sourced by the fluid velocity. The 'TE' part of the polarization and temperature patterns comes from correlations between density and velocity perturbations on the last scattering surface, which can be both positive and negative, and is of larger amplitude than the EE signal. There is no polarization Sachs-Wolfe effect, and hence no large-angle plateau. However, scattering during a recent period of reionization can create a polarization 'bump' at large angular scales.

Because the polarization anisotropies have only a fraction of the amplitude of the temperature anisotropies, they took longer to detect. The first measurement of a polarization signal came in 2002 from the DASI experiment [57], which provided a convincing detection, confirming the general paradigm, but of low enough significance that it lent little constraint to models. Despite dramatic progress since then, it is still the case that polarization data mainly support the basic paradigm, without dramatically reducing error bars on parameters. However, there are exceptions to this, specifically in the reionization optical depth, and the potential to constrain primordial gravitational waves.

28.7.1. *T–E Power Spectrum* :

Since the T and E skies are correlated, one has to measure the TE power spectrum, as well as TT and EE, in order to extract all the cosmological information. This TE signal has now been mapped out extremely accurately by *Planck* [51], and these band-powers are shown in Fig. 28.3, along with those from *WMAP* [58] and BICEP2/Keck [59], with ACT [60] and SPT [61] extending to smaller angular scales. The anti-correlation at $\ell \simeq 150$ and the peak at $\ell \simeq 300$ were the first features to become distinct, but now a whole series of oscillations is clearly seen in this power spectrum. The measured shape of the cross-correlation power spectrum provides supporting evidence for the general cosmological picture, as well as directly constraining the thickness of the last scattering surface. Since the polarization anisotropies are generated in this scattering surface, the existence of correlations at angles above about a degree demonstrates that there were super-Hubble fluctuations at the recombination epoch. The sign of this correlation also

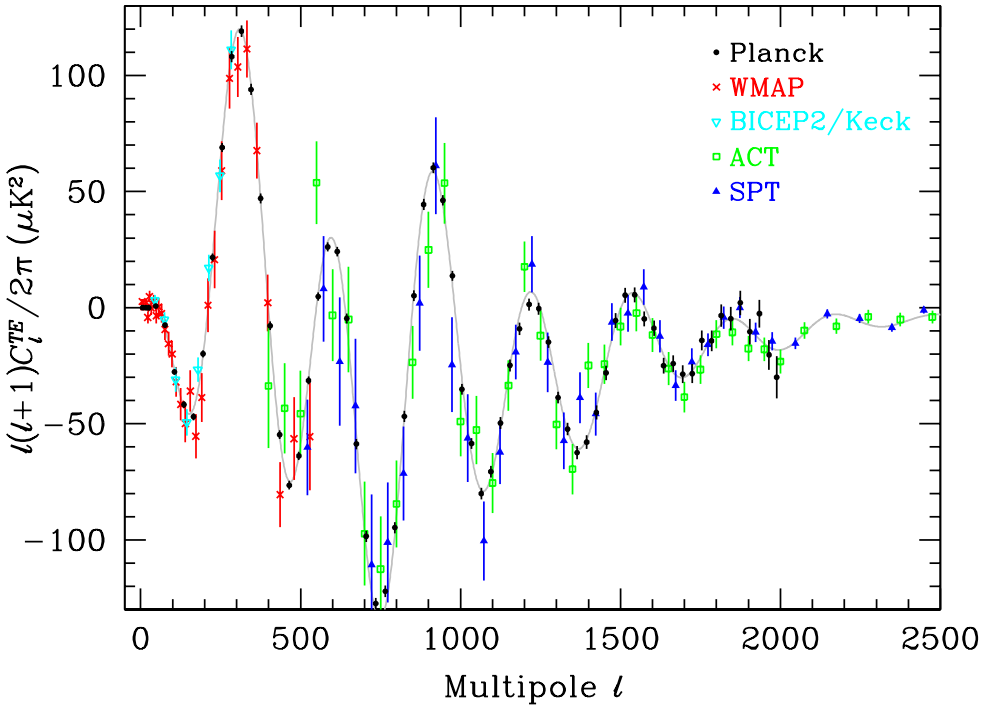

Figure 28.3: Cross-power spectrum band-powers of the temperature anisotropies and E-mode polarization signal from *Planck* (the low multipole data have been binned here), *WMAP*, BICEP2/Keck, ACT, and SPT. The curve is the prediction from the best fit to the *Planck* temperature band-powers (as well as the $\ell < 30$ polarization and CMB lensing results) and is not a fit to these data; however, these TE measurements follow the curve very closely, showing the expected oscillatory structure. Note that each band-power is an average over a range of multipoles, and hence to compare in detail with a model one has to average the theoretical curve through the band.

confirms the adiabatic paradigm.

The overall picture of the source of CMB polarization and its oscillations has also been confirmed through tests that average the maps around both temperature hot spots and cold spots [62,11]. One sees precisely the expected patterns of radial and tangential polarization configurations, as well as the phase shift between polarization and temperature. This leaves no doubt that the oscillation picture is the correct one and that the polarization is coming from Thomson scattering at $z \simeq 1100$.

28.7.2. *E–E Power Spectrum* :

Experimental band-powers for C_ℓ^{EE} from *Planck*, *WMAP*, BICEP2/Keck Array [59] , QUAD [63], ACT [60], and SPT [61] are shown in Fig. 28.4. Without the benefit of correlating with the temperature anisotropies (*i.e.*, measuring C_ℓ^{TE}), the polarization anisotropies are very weak and challenging to measure. Nevertheless, the oscillatory pattern is becoming well established and the data closely match the TT-derived theoretical prediction. In Fig. 28.4 one can clearly see the 'shoulder' expected at $\ell \simeq 140$, the first

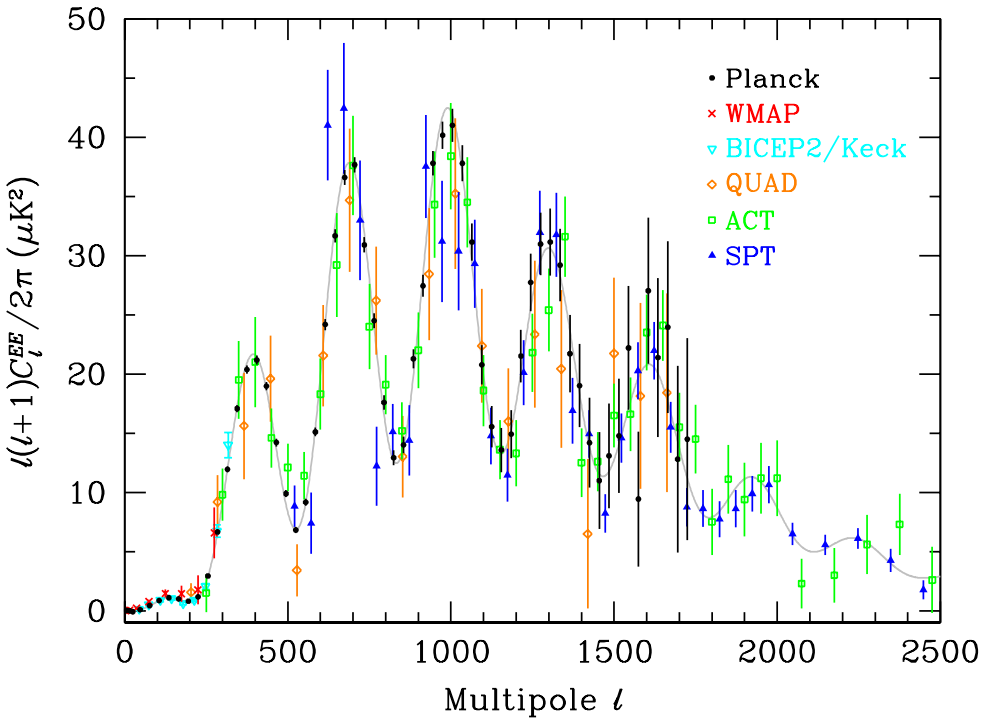

Figure 28.4: Power spectrum of E-mode polarization from *Planck*, together with *WMAP*, BICEP2/Keck, QUAD, ACT, and SPT. Note that some band-powers with larger uncertainties have been omitted and that the unbinned *Planck* low-ℓ data have been binned here. Also plotted is the best-fit theoretical model from *Planck* TT data (plus polarization at $\ell < 30$ and CMB lensing).

main peak at $\ell \simeq 400$ (corresponding to the first trough in C_ℓ^{TT}), and the series of oscillations that is out of phase with the temperature anisotropy power spectrum.

Perhaps the most distinctive result from the polarization measurements is at the largest angular scales ($\ell < 10$) in C_ℓ^{TE} and C_ℓ^{EE}, where there is evidence for an excess signal (not visible in Fig. 28.4) compared to that expected from the temperature power spectrum alone. This is precisely the signal anticipated from an early period of reionization, arising from Doppler shifts during the partial scattering at $z < z_{\rm i}$. The amplitude of the signal indicates that the first stars, presumably the source of the ionizing radiation, formed around $z \simeq 10$ (although the uncertainty is still quite large). Since this corresponds to scattering optical depth $\tau \simeq 0.1$, then roughly 10% of CMB photons were re-scattered at the reionization epoch, with the other 90% last scattering at $z \simeq 1100$. However, estimates of the amplitude of this reionization excess have come down since the first measurements by *WMAP* (indicating that this is an extremely difficult measurement to make) and the latest determination from *Planck* gives $z_{\rm i} = 8.8^{+1.7}_{-1.4}$ [13].

28.7.3. ***B–B Power Spectrum*** :

The expected amplitude of C_ℓ^{BB} is very small, and so measurements of this polarization curl-mode are very challenging. The first indication of the existence of the BB signal has come from the detection of the expected conversion of E-modes to B-modes by gravitational lensing, through a correlation technique using the lensing potential and polarization measurements from SPT [64]. However, the real promise of B-modes lies in the detection of primordial gravitational waves at larger scales. This tensor signature could be seen either in the 'recombination bump' at around $\ell = 100$ (caused by an ISW effect as gravitational waves redshift away at the last-scattering epoch) or the 'reionization bump' (from additional scattering at low redshifts).

Results from the BICEP-2 experiment [65] in 2014 suggested a detection of the primordial B-mode signature around the recombination peak. BICEP-2 mapped a small part of the CMB sky with the the lowest sensitivity level yet reached (below 100 nK), but at a single frequency. Higher frequency data from *Planck* indicated that much of the BICEP2 signal was due to dust within out Galaxy, and a combined analysis by the BICEP-2, Keck Array, and *Planck* teams [66] indicated that the data are consistent with no primordial B-modes, with an upper limit of $r < 0.12$.

Several experiments are continuing to push down the sensitivity of B-mode measurements, motivated by the enormous importance of a future detection of this telltale signature of inflation (or other physics at the highest energies). A compilation of experimental results for C_ℓ^{BB} is shown in Fig. 28.5, coming from a combination of direct estimates of the B-modes (BICEP2/Keck Array [59], POLARBEAR [67], and SPTpol [68]) and indirect determinations of the lensing B-modes based on estimating the effect of measured lensing on measured E-modes (*Planck* [48], SPT [64], and ACT [69]). Additional band-power estimates are expected from these and other experiments in the near future.

28.8. Complications

There are a number of issues that complicate the interpretation of CMB anisotropy data (and are considered to be *signal* by many astrophysicists), some of which we sketch out below.

28.8.1. ***Foregrounds*** :

The microwave sky contains significant emission from our Galaxy and from extra-galactic sources [70]. Fortunately, the frequency dependence of these various sources is in general substantially different from that of the CMB anisotropy signals. The combination of Galactic synchrotron, bremsstrahlung, and dust emission reaches a minimum at a frequency of roughly 100 GHz (or wavelength of about 3 mm). As one moves to greater angular resolution, the minimum moves to slightly higher frequencies, but becomes more sensitive to unresolved (point-like) sources.

At frequencies around 100 GHz, and for portions of the sky away from the Galactic Plane, the foregrounds are typically 1 to 10% of the CMB anisotropies. By making observations at multiple frequencies, it is relatively straightforward to separate the various components and determine the CMB signal to the few per cent level. For greater sensitivity, it is necessary to use the spatial information and statistical properties of the

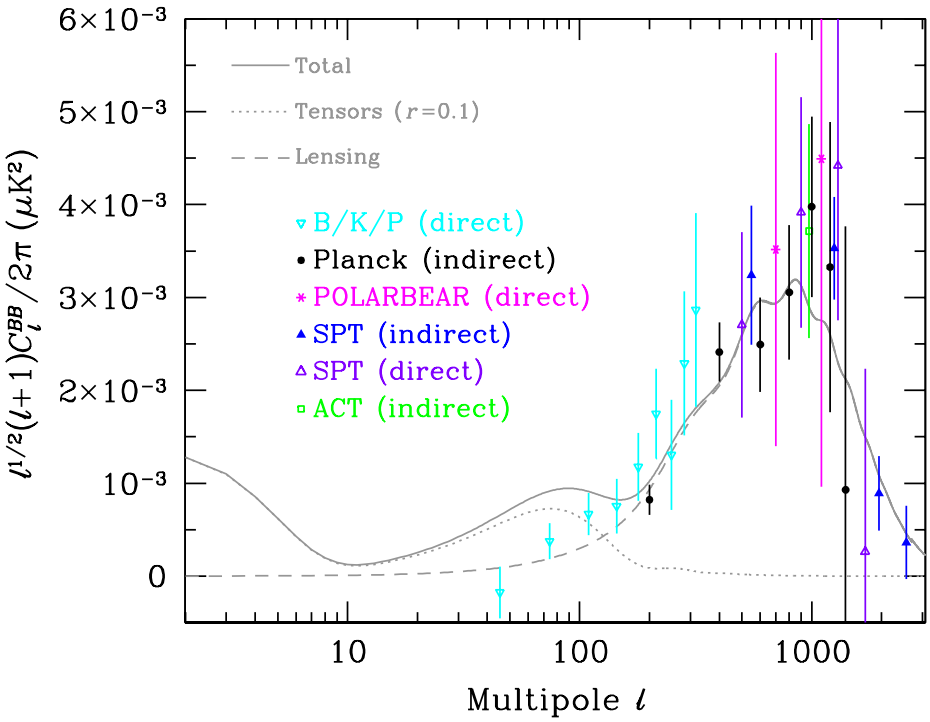

Figure 28.5: Power spectrum of B-mode polarization, including results from the BICEP2/Keck Array/*Planck* combined analysis (B/K/P), *Planck*, POLARBEAR, SPT, and ACT. Note that some of the measurements are direct estimates of B-modes on the sky, while others are only sensitive to the lensing signal and come from combining E-mode and lensing potential measurements. Several experiments have previous reported upper limits, which are all off the top of this plot. A logarithmic x-axis is adopted here and the y-axis has been divided by a factor of $\sqrt{\ell}$ in order to show all three theoretically expected contributions: the low-ℓ reionization bump; the $\ell \sim 100$ recombination peak; and the high-ℓ lensing signature. The dotted line is for a tensor (primordial gravitational wave) fraction $r = 0.1$, simply as an example, with all other cosmological parameters set at the best *Planck*-derived values, for which model the expected lensing B-modes have also been shown with a dashed line.

foregrounds to separate them from the CMB. Furthermore, at higher ℓs it is essential to carefully model extragalactic foregrounds, particularly the clustering of infrared-emitting galaxies, which dominate the measured power spectrum as we move into the damping tail.

The foregrounds for CMB polarization follow a similar pattern to those for temperature, but are less well studied, and are intrinsically brighter relative to CMB anisotropies. *WMAP* showed that the polarized foregrounds dominate at large angular scales, and that they must be well characterized in order to be discriminated [71]. *Planck* has shown that it is possible to characterize the foreground polarization signals, with synchrotron dominating at low frequencies and dust at high frequencies [72]. Whether the foregrounds become more complicated as we push down in sensitivity at high multipoles is not known. However, although they make analysis more difficult, for the

time being, foreground contamination is not a fundamental limit for CMB experiments.

28.8.2. ***Secondary Anisotropies*** :

With increasingly precise measurements of the primary anisotropies, there is growing theoretical and experimental interest in 'secondary anisotropies,' pushing experiments to higher angular resolution and sensitivity. These secondary effects arise from the processing of the CMB due to ionization history and the evolution of structure, including gravitational lensing (which was already discussed) and patchy reionization effects [73] . Additional information can thus be extracted about the Universe at $z \ll 1000$. This tends to be most effectively done through correlating CMB maps with other cosmological probes of structure. Secondary signals are also typically non-Gaussian, unlike the primary CMB anisotropies.

A secondary signal of great current interest is the Sunyaev-Zeldovich (SZ) effect [74], which is Compton scattering ($\gamma e \rightarrow \gamma' e'$) of the CMB photons by hot electron gas. This creates spectral distortions by transferring energy from the electrons to the photons. It is particularly important for clusters of galaxies, through which one observes a partially Comptonized spectrum, resulting in a decrement at radio wavelengths and an increment in the submillimeter.

The imprint on the CMB sky is of the form $\Delta T/T = y\, f(x)$, with the y-parameter being the integral of Thomson optical depth times $kT_{\rm e}/m_{\rm e}c^2$ through the cluster, and $f(x)$ describing the frequency dependence. This is simply $x\coth(x/2) - 4$ for a non-relativistic gas (the electron temperature in a cluster is typically a few keV), where the dimensionless frequency $x \equiv h\nu/kT_\gamma$. As well as this 'thermal' SZ effect, there is also a smaller 'kinetic' effect due to the bulk motion of the cluster gas, giving $\Delta T/T \sim \tau(v/c)$, with either sign, but having the same spectrum as the primary CMB anisotropies.

A significant advantage in finding galaxy clusters this way is that the SZ effect is largely independent of redshift, so in principle clusters can be found to arbitrarily large distances. The SZ effect can be used to find and study individual clusters, and to obtain estimates of the Hubble constant. There is also the potential to constrain cosmological parameters, such as the clustering amplitude σ_8 and the equation of state of the dark energy, through counts of detected clusters as a function of redshift. The promise of the method has been realized through detections of clusters purely through the SZ effect by SPT [75], ACT [76], and *Planck* [77]. Results from *Planck* clusters [78] suggest a somewhat lower value of σ_8 than inferred from CMB anisotropies, but there are still systematic uncertainties that might encompass the difference. Further analysis of scaling relations among cluster properties should enable more robust cosmological constraints to be placed in future, so that we can understand whether this 'tension' might be a sign of new physics.

28.8.3. *Higher-order Statistics* :

Although most of the CMB anisotropy information is contained in the power spectra, there will also be weak signals present in higher-order statistics. These can measure any primordial non-Gaussianity in the perturbations, as well as non-linear growth of the fluctuations on small scales and other secondary effects (plus residual foreground contamination of course). Although there are an infinite variety of ways in which the CMB could be non-Gaussian [29], there is a generic form to consider for the initial conditions, where a quadratic contribution to the curvature perturbations is parameterized through a dimensionless number $f_{\rm NL}$. This weakly non-linear component can be constrained in several ways, the most popular being through measurements of the bispectrum.

The constraints depend on the shape of the triangles in harmonic space, and it has become common to distinguish the 'local' or 'squeezed' configuration (in which one side is much smaller than the other two) from the 'equilateral' configuration. Other configurations are also relevant for specific theories, such as 'orthogonal' non-Gaussianity, which has positive correlations for $k_1 \simeq 2k_2 \simeq 2k_3$, and negative correlations for the equilateral configuration. The results from the *Planck* team [79](including polarization here) are $f_{\rm NL}^{\rm local} = 1 \pm 5$, $f_{\rm NL}^{\rm equil} = 0 \pm 40$, and $f_{\rm NL}^{\rm ortho} = -26 \pm 21$.

These results are consistent with zero, but are at a level that is now interesting for model predictions. The amplitude of $f_{\rm NL}$ expected is small, so that a detection of $f_{\rm NL} \gg 1$ would rule out all single-field, slow-roll inflationary models. It is still possible to improve upon these *Planck* results, and it certainly seems feasible that a measurement of primordial non-Gaussianity may yet be within reach. *Non*-primordial detections of non-Gaussianity from expected signatures have already been made. For example, the bispectrum and trispectrum contain evidence of gravitational lensing, the ISW effect, and Doppler boosting. For now the primordial signal is elusive, but should it be detected, then detailed measurements of non-Gaussianity will become a unique probe of inflationary-era physics. Because of that, much effort continues to be devoted to honing predictions and measurement techniques, with the expectation that we will need to go beyond the CMB to dramatically improve the constraints.

28.8.4. *Anomalies* :

Several features seen in the *Planck* data [32] confirm those found earlier with *WMAP* [31], showing mild deviations from a simple description of the data; these are often referred to as 'anomalies.' One such feature is the apparent lack of power in the multipole range $\ell \simeq 20$–30 [9,51]. The other examples involve the breaking of statistical anisotropy, caused by alignment of the lowest multipoles, or a somewhat excessive cold spot, or a power asymmetry between hemispheres. No such feature is significant at more than the roughly 3σ level, and the importance of 'a posteriori' statistics here has been emphasized by many authors. Since these effects are at large angular scales, where cosmic variance dominates, the results will not increase in significance with more data, although there is the potential for polarization data to provide independent tests.

28.9. Constraints on Cosmological Parameters

The most striking outcome of the newer experimental results is that the standard cosmological paradigm is in very good shape. A large amount of high precision data on the power spectrum is adequately fit with fewer than 10 free parameters (and only six need non-trivial values). The framework is that of FRW models, which have nearly flat geometry, containing dark matter and dark energy, and with adiabatic perturbations having close to scale-invariant initial conditions.

Within this basic picture, the values of the cosmological parameters can be constrained. Of course, much more stringent bounds can be placed on models that cover a restricted parameter space, *e.g.*, assuming that $\Omega_{\rm tot} = 1$ or $r = 0$. More generally, the constraints depend upon the adopted prior probability distributions, even if they are implicit, for example by restricting the parameter freedom or their ranges (particularly where likelihoods peak near the boundaries), or by using different choices of other data in combination with the CMB. As the data become even more precise, these considerations will be less important, but for now we caution that restrictions on model space and choice of non-CMB data-sets and priors need to be kept in mind when adopting specific parameter values and uncertainties.

There are some combinations of parameters that fit the CMB anisotropies almost equivalently. For example, there is a nearly exact geometric degeneracy, where any combination of $\Omega_{\rm m}$ and Ω_Λ that gives the same angular diameter distance to last scattering will give nearly identical C_ℓs. There are also other less exact degeneracies among the parameters. Such degeneracies can be broken when using the CMB results in combination with other cosmological data-sets. Particularly useful are complementary constraints from baryon acoustic oscillations, galaxy clustering, the abundance of galaxy clusters, weak gravitational lensing measurements, and Type Ia supernova distances. For an overview of some of these other cosmological constraints, see The Cosmological Parameters—Sec. 25 of this *Review*.

Within the context of a six parameter family of models (which fixes $\Omega_{\rm tot} = 1$, $dn_{\rm s}/d\ln k = 0$, $r = 0$, and $w = -1$) the *Planck* results for TT, together with low-ℓ polarization and CMB lensing, and the use of high-ℓ data from ACT and SPT to constrain foregrounds, yields [13]: $\ln(10^{10}A_{\rm s}) = 3.062 \pm 0.029$; $n_{\rm s} = 0.968 \pm 0.006$; $\Omega_{\rm b}h^2 = 0.02226 \pm 0.00023$; $\Omega_{\rm c}h^2 = 0.1186 \pm 0.0020$; $100\theta_* = 1.0410 \pm 0.0005$; and $\tau = 0.066 \pm 0.016$. Other parameters can be derived from this basic set, including $h = 0.678 \pm 0.009$, $\Omega_\Lambda = 0.692 \pm 0.012$ $(= 1 - \Omega_{\rm m})$ and $\sigma_8 = 0.815 \pm 0.009$. Somewhat different (although consistent) values are obtained using other data combinations, such as including BAO, supernova, H_0, or weak lensing constraints (see Sec. 25 of this *Review*). However, the results quoted above are currently the best available from CMB anisotropies alone. The uncertainties decrease by around 25% when adding *Planck* polarization data, although the recommendation for now is not to include these 2015 polarization data in fits, since there are still some unmodeltaed systematic effects present [51].

The standard cosmological model continues to fit the data well, with the error bars on the parameters continuing to shrink. Improved measurement of higher acoustic peaks has dramatically reduced the uncertainty in the θ_* parameter, which is now detected at $> 2000\sigma$. The evidence for $n_{\rm s} < 1$ remains above the 5σ level. The value of the reionization optical depth has decreased compared with earlier estimates; it is

convincingly detected, but still not of very high significance.

Constraints can also be placed on parameters beyond the basic six, particularly when including other astrophysical data-sets. Relaxing the flatness assumption, the constraint on $\Omega_{\rm tot}$ is 1.005 ± 0.008. Note that for h, the CMB data alone provide only a very weak constraint if spatial flatness is not assumed. However, with the addition of other data (particularly powerful in this context being a compilation of BAO measurements [80]), the constraints on the Hubble constant and curvature improve considerably, leading to $\Omega_{\rm tot} = 1.0002 \pm 0.0026$ [13].

For $\Omega_{\rm b}h^2$ the CMB-derived value is generally consistent with completely independent constraints from Big Bang nucleosynthesis (see Sec. 24 of this *Review*). Related are constraints on additional neutrino-like relativistic degrees of freedom, which lead to $N_{\rm eff} = 3.15 \pm 0.23$ (including BAO), *i.e.*, no evidence for extra neutrino species.

The 95% confidence upper limit on r (measured at $k = 0.002\,{\rm Mpc}^{-1}$) from the effect of tensors solely on C_ℓ^{TT} (see Fig. 28.1) is 0.11. This limit depends on how the slope n is restricted and whether $dn_{\rm s}/d\ln k \neq 0$ is allowed. The joint constraints on $n_{\rm s}$ and r allows specific inflationary models to be tested [33,34]. The limit on r is even tighter when combined with the BICEP/Keck/*Planck* results for C_ℓ^{BB}, yielding $r < 0.08$ at 95% confidence [34]. Looking at the $(n_{\rm s}, r)$ plane, this means that $m^2\phi^2$ (mass-term quadratic) inflation is now disfavored by the data, as well as $\lambda\phi^4$ (self-coupled) inflation.

The addition of the dark energy equation of state w adds the partial degeneracy of being able to fit a ridge in (w, h) space, extending to low values of both parameters. This degeneracy is broken when the CMB is used in combination with other data-sets, *e.g.*, adding a compilation of BAO data gives $w = -1.01 \pm 0.05$. Constraints can also be placed on more general dark energy and modified gravity models [81]. However, one needs to be careful not to over-interpret some tensions between data-sets as evidence for new physics.

For the optical depth τ, the best-fit corresponds to a reionization redshift centered on 9 in the best-fit cosmology, and assuming instantaneous reionization. This redshift is only slightly higher that that suggested from studies of absorption lines in high-z quasar spectra [82] and Ly α-emitting galaxies [83], perhaps hinting that the process of reionization was not as complex as previously suspected. The important constraint provided by CMB polarization, in combination with astrophysical measurements, thus allows us to investigate how the first stars formed and brought about the end of the cosmic dark ages.

28.10. Particle Physics Constraints

CMB data place limits on parameters that are directly relevant for particle physics models. For example, there is a limit on the sum of the masses of the neutrinos, $\sum m_\nu < 0.21\,{\rm eV}$ (95%) [9] coming from *Planck* together with BAO measurements (although limits are weaker when considering both $N_{\rm eff}$ and $\sum m_\nu$ as free parameters). This assumes the usual number density of fermions, which decoupled when they were relativistic. The limit is tantalizingly only a factor of a few higher than the minimum value coming from neutrino mixing experiments (see Neutrino Mixings—Sec. 14). As well as being an indirect probe of the neutrino background, *Planck* data also require that the

neutrino background has perturbations, i.e. that it possesses a sound speed $c_{\rm s}^2 \simeq 1/3$, as expected [13].

The current suite of data suggests that $n_{\rm s} < 1$, with a best-fitting value about 0.03 below unity. This is already quite constraining for inflationary models, particularly along with r limits. There is no current evidence for running of the spectral index, with $dn_{\rm s}/d\ln k = -0.003 \pm 0.008$ from *Planck* alone [13], although this is less of a constraint on inflationary models. Similarly, primordial non-Gaussianity is being probed to interesting levels, although tests of simple inflationary models will only come with significant reductions in uncertainty.

The large-angle anomalies, such as the hemispheric modulation of power and the dip in power at $\ell \simeq 20$–30, have the potential to be hints of new physics. Such effects might be expected in a universe that has a large-scale power cut-off, or anisotropy in the initial power spectrum, or is topologically non-trivial. However, cosmic variance and *a posteriori* statistics limit the significance of these anomalies, absent the existence of a model that naturally yields some of these features (and hopefully also predicting other phenomena that can be tested).

It is possible to place limits on additional areas of physics [84], for example annihilating dark matter, [13], primordial magnetic fields [85], and time variation of the fine-structure constant [86], as well as parity violation, the neutrino chemical potential, a contribution of warm dark matter, topological defects, or physics beyond general relativity. Further particle physics constraints will follow as the anisotropy measurements increase in precision.

The CMB anisotropy measurements precisely pin down physics at the time of last-scattering, and so any change of physics can be constrained if it affects the relevant energies or timescales. Future, higher sensitivity measurements of the CMB frequency spectrum will push the constraints back to cover energy injection at much earlier times ($\sim 1\,$year). Comparison of CMB and BBN observables extend these constraints to timescales of order seconds, and energies in the MeV range. And to the extent that inflation provides an effective description of the generation of perturbations, the inflationary observables will constrain physics at GUT-type energy scales.

More generally, careful measurement of the CMB power spectra and non-Gaussianity can in principle put constraints on physics at the highest energies, including ideas of string theory, extra dimensions, colliding branes, *etc.* At the moment any calculation of predictions appears to be far from definitive. However, there is a great deal of activity on implications of string theory for the early Universe, and hence a very real chance that there might be observational implications for specific scenarios.

28.11. Fundamental Lessons

More important than the precise values of parameters is what we have learned about the general features that describe our observable Universe. Beyond the basic hot Big Bang picture, the CMB has taught us that:

- The Universe recombined at $z \simeq 1100$ and started to become ionized again at $z \simeq 10$.
- The geometry of the Universe is close to flat.
- Both dark matter and dark energy are required.

- Gravitational instability is sufficient to grow all of the observed large structures in the Universe.
- Topological defects were not important for structure formation.
- There are 'synchronized' super-Hubble modes generated in the early Universe.
- The initial perturbations were predominantly adiabatic in nature.
- The perturbation spectrum has a slightly red tilt.
- The perturbations had close to Gaussian (*i.e.*, maximally random) initial conditions.

These features form the basis of the cosmological standard model, ΛCDM, for which it is tempting to make an analogy with the Standard Model of particle physics (see earlier Sections of this *Review*). The cosmological model is much further from any underlying 'fundamental theory,' which may ultimately provide the values of the parameters from first principles. Nevertheless, any genuinely complete 'theory of everything' must include an explanation for the values of these cosmological parameters as well as the parameters of the Standard Model of particle physics.

28.12. Future Directions

Given the significant progress in measuring the CMB sky, which has been instrumental in tying down the cosmological model, what can we anticipate for the future? There will be a steady improvement in the precision and confidence with which we can determine the appropriate cosmological parameters. Ground-based experiments operating at smaller angular scales will continue to place tighter constraints on the damping tail. New polarization experiments at small scales will probe further into the damping tail, without the limitation of extragalactic foregrounds. And polarization experiments at large angular scales will push down the limits on primordial B-modes.

Planck, the third generation CMB satellite mission, was launched in May 2009, and has produced a large number of papers, including a set of cosmological studies based on the first two full surveys of the sky (accompanied by a public release of data products) in 2013 and a further series based on analysis of the full mission data release in 2015 (eight surveys for the Low Frequency Instrument and five surveys for the High Frequency Instrument). In 2016 results are expected from a final analysis, including a comprehensive investigation of polarization.

A set of cosmological parameters is now known to percent level accuracy, and that may seem sufficient for many people. However, we should certainly demand more of measurements that describe *the entire observable Universe!* Hence a lot of activity in the coming years will continue to focus on determining those parameters with increasing precision. This necessarily includes testing for consistency among different predictions of the cosmological Standard Model, and searching for signals that might require additional physics.

A second area of focus will be the smaller scale anisotropies and 'secondary effects.' There is a great deal of information about structure formation at $z \ll 1000$ encoded in the CMB sky. This may involve higher-order statistics and cross-correlations with other large-scale structure tracers, as well as spectral signatures, with many experiments targeting the galaxy cluster SZ effect. The current status of CMB lensing is similar (in

terms of total signal-to-noise) to the quality of the first CMB anisotropy measurements by *COBE*, and thus we can expect that experimental probes of lensing will improve dramatically in the coming years. All of these investigations can provide constraints on the dark energy equation of state, for example, which is a major area of focus for several future cosmological surveys at optical wavelengths. CMB lensing also promises to yield a measurement of the sum of the neutrino masses.

A third direction is increasingly sensitive searches for specific signatures of physics at the highest energies. The most promising of these may be the primordial gravitational wave signals in C_ℓ^{BB}, which could be a probe of the $\sim 10^{16}$ GeV energy range. There are several ground- and balloon-based experiments underway that are designed to search for the polarization B-modes. Additionally, non-Gaussianity holds the promise of constraining models beyond single-field slow-roll inflation.

Anisotropies in the CMB have proven to be the premier probe of cosmology and the early Universe. Theoretically the CMB involves well understood physics in the linear regime, and is under very good calculational control. A substantial and improving set of observational data now exists. Systematics appear to be under control and not a limiting factor. And so for the next few years we can expect an increasing amount of cosmological information to be gleaned from CMB anisotropies, with the prospect also of some genuine surprises.

References:

1. A.A. Penzias and R. Wilson, Astrophys. J. **142**, 419 (1965);
   R.H. Dicke *et al.*, Astrophys. J. **142**, 414 (1965).
2. M. White, D. Scott, and J. Silk, Ann. Rev. Astron. Astrophys. **32**, 329 (1994);
   W. Hu and S. Dodelson, Ann. Rev. Astron. Astrophys. **40**, 171 (2002);
   A. Challinor and H. Peiris, Proc. Astro. Soc. Pacific Conf. Ser. Vol. 1132, 86 (2009).
3. G.F. Smoot *et al.*, Astrophys. J. **396**, L1 (1992).
4. C.L. Bennett *et al.*, Astrophys. J. Supp. **148**, 1 (2003).
5. N. Jarosik *et al.*, Astrophys. J. Supp. **170**, 263 (2007).
6. G. Hinshaw *et al.*, Astrophys. J. Supp. **180**, 225 (2009).
7. N. Jarosik *et al.*, Astrophys. J. Supp. **192**, 14 (2011).
8. G. Hinshaw *et al.*, Astrophys. J. Supp. **208**, 19 (2013).
9. Planck Collab. 2013 Results XVI, Astron. & Astrophys. **571**, A16 (2014).
10. J.A. Tauber *et al.*, Astron. & Astrophys. **520**, 1 (2010);
    Planck Collab. Early Results I, Astron. & Astrophys. **536**, 1 (2011).
11. Planck Collab. 2013 Results I, Astron. & Astrophys. **571**, A1 (2014).
12. Planck Collab. 2015 Results I, Astron. & Astrophys. submitted, `arXiv:1502.01582`.
13. Planck Collab. 2015 Results XIII, Astron. & Astrophys. submitted, `arXiv:1502.01589`.
14. D.S. Swetz *et al.*,Astrophys. J. Supp. **194**, 41 (2011).
15. J.E. Carlstron *et al.*, Publ. Astron. Soc. Pacific **123**, 568 (2011).
16. P. Noterdaeme *et al.*, Astron. & Astrophys. **526**, L7 (2011).
17. D.J. Fixsen *et al.*, Astrophys. J. **734**, 5 (2011).
18. R. Subrahmanyan and R. Cowsik, Astrophys. J. **776**, 42 (2013).
19. A. Kogut *et al.*, Proc. SPIE, vol. 9143, 1E (2014).

20. R. Khatri and R.A. Sunyaev, JCAP **6**, 026 (2013);
J. Chluba and D. Jeong, MNRAS **438**, 2065 (2014).
21. D.J. Fixsen, Astrophys. J. **707**, 916 (2009).
22. J.C. Mather *et al.*, Astrophys. J. **512**, 511 (1999).
23. Y. Hoffman, H.M. Courtois, and R.B. Tully, MNRAS **449**, 4494 (2015).
24. D.J. Fixsen *et al.*, Astrophys. J. **420**, 445 (1994).
25. Planck Collab. 2013 Results XXVII, Astron. & Astrophys. **571**, A27 (2014).
26. A. Kogut *et al.*, Astrophys. J. **419**, 1 (1993).
27. S. Seager, D.D. Sasselov, and D. Scott, Astrophys. J. Supp. **128**, 407 (2000).
28. L. Knox, Phys. Rev. **D52**, 4307 (1995).
29. N. Bartolo *et al.*, Phys. Reports **402**, 103 (2004);
E. Komatsu, Class. Quantum Grav. **27**, 124010 (2010);
A.P.S. Yadav and B.D. Wandelt, Adv. Astron. **2010**, 565248 (2010).
30. Planck Collab. 2013 Results XXIV, Astron. & Astrophys. **571**, A24 (2014).
31. C.L. Bennett *et al.*, Astrophys. J. Supp. **192**, 17 (2011).
32. Planck Collab. 2013 Results XXIII, Astron. & Astrophys. **571**, A23 (2014);
Planck Collab. 2015 Results XXIII, Astron. & Astrophys. submitted, `arXiv:1506.07135`.
33. Planck Collab. 2013 Results XXII, Astron. & Astrophys. **571**, A22 (2014).
34. Planck Collab. 2015 Results XX, Astron. & Astrophys. submitted, `arXiv:1502.02114`.
35. A.R. Liddle and D.H. Lyth, Cosmological Inflation and Large-Scale Structure, Cambridge University Press (2000).
36. U. Seljak and M. Zaldarriaga, Astrophys. J. **469**, 437 (1996).
37. A. Lewis, A. Challinor, and A. Lasenby, Astrophys. J. **538**, 473 (2000).
38. U. Seljak *et al.*, Phys. Rev. **D68**, 083507 (2003);
C. Howlett *et al.*, JCAP **04**, 027 (2012).
39. R.K. Sachs and A.M. Wolfe, Astrophys. J. **147**, 73 (1967).
40. R. Crittenden and N. Turok, Phys. Rev. Lett. **76**, 575 (1996);
Planck Collab. 2015 Results XXI, Astron. & Astrophys. submitted, `arXiv:1502.01595`.
41. W. Hu *et al.*, Phys. Rev. **D59**, 023512 (1999).
42. P.J.E. Peebles and J.T. Yu, Astrophys. J. **162**, 815 (1970);
R.A. Sunyaev and Ya.B. Zeldovich, Astrophys. & Space Sci. **7**, 3 (1970).
43. D. Scott, J. Silk, and M. White, Science **268**, 829 (1995).
44. D.J. Eisenstein, New Astron. Rev. **49**, 360 (2005);
W.J. Percival *et al.*, MNRAS **381**, 1053 (2007).
45. J. Silk, Astrophys. J. **151**, 459 (1968).
46. M. Zaldarriaga and U. Seljak, Phys. Rev. **D58**, 023003 (1998);
A. Lewis and A. Challinor, Phys. Reports **429**, 1 (2006).
47. Planck Collab. 2013 Result XVII, Astron. & Astrophys. **571**, A17 (2014).
48. Planck Collab. 2015 Results XV, Astron. & Astrophys. submitted, `arXiv:1502.01591`.
49. M. Kaplighat, L. Knox, and Y.-S. Song, Phys. Rev. Lett. **91**, 241301 (2003).
50. Planck Collab. 2013 Results XV, Astron. & Astrophys. **571**, A15 (2014).
51. Planck Collab. 2015 Results XI, Astron. & Astrophys. submitted, `arXiv:1507.07283`.
52. S. Das *et al.*, JCAP **04**, 014 (2014).

53. R. Keisler *et al.*, Astrophys. J. **743**, 28 (2011);
C.L. Reichardt *et al.*, Astrophys. J. **755**, 70 (2012);
K.T. Story *et al.*, Astrophys. J. **779**, 86 (2013).
54. W. Hu and M. White, New Astron. **2**, 323 (1997).
55. W. Hu and M. White, Phys. Rev. **D56**, 596 (1997).
56. M. Zaldarriaga and U. Seljak, Phys. Rev. **D55**, 1830 (1997);
M. Kamionkowski, A. Kosowsky, and A. Stebbins, Phys. Rev. **D55**, 7368 (1997).
57. J. Kovac *et al.*, Nature **420**, 772 (2002).
58. D. Larson *et al.*, Astrophys. J. Supp. **192**, 16 (2011).
59. Keck Array V and BICEP2 Collabs, P.A.R. Ade *et al.*, Astrophys. J. **811**, 126, (2015).
60. S. Naess *et al.*, JCAP **10**, 007 (2014).
61. A.T. Crites *et al.*, Astrophys. J. **805**, 36 (2015).
62. E. Komatsu *et al.*, Astrophys. J. Supp. **192**, 18 (2011).
63. M.L. Brown *et al.*, Astrophys. J. **705**, 978 (2009).
64. D. Hanson *et al.*, Phys. Rev. Lett. **111**, 141301 (2013) arXiv:1307.5830.
65. BICEP2 Collab., Phys. Rev. Lett. **112**, 1101 (2014).
66. BICEP/Keck and Planck Collabs., Phys. Rev. Lett. **114**, 1301 (2015).
67. POLARBEAR Collab., Astrophys. J. **794**, 171 (2014).
68. R. Keisler *et al.*, Astrophys. J. **807**, 151 (2015).
69. A. van Engelen *et al.*, Astrophys. J. **808**, 7 (2015).
70. Planck Collab. 2013 Results XII, Astron. & Astrophys. **571**, A12 (2014);
Planck Collab. 2015 Results IX, Astron. & Astrophys. submit., arXiv:1502.05956;
Planck Collab. 2015 Results X, Astron. & Astrophys. submitted, arXiv:1502.01588.
71. B. Gold *et al.*, Astrophys. J. Supp. **192**, 15 (2011).
72. Planck Collab. Interm. Results XXX, Astron. & Astrophys. submitted, arXiv:1409.5738;
Planck Collab. 2015 Results XII, Astron. & Astrophys. submitted, arXiv:1506.06660.
73. M. Millea *et al.*, Astrophys. J. **746**, 4 (2012);
E. Calabrese *et al.*, JCAP **8**, 010 (2014).
74. R.A. Sunyaev and Ya.B. Zeldovich, Ann. Rev. Astron. Astrophys. **18**, 537 (1980);
M. Birkinshaw, Phys. Reports **310**, 98 (1999);
J.E. Carlstrom, G.P. Holder, and E.D. Reese, Ann. Rev. Astron. Astrophys. **40**, 643 (2002).
75. R. Williamson *et al.*, Astrophys. J. **738**, 139 (2011);
L.E. Bleem *et al.*, Astrophys. J. Supp. **216**, 27 (2015).
76. T.A. Marriage *et al.*, Astrophys. J. **737**, 61 (2011);
M. Hasselfield *et al.*, JCAP **07**, 008 (2013).
77. Planck Collab. Early Results VIII, Astron. & Astrophys. **536**, 8 (2011);
Planck Collab. 2013 Results XXIX, Astron. & Astrophys. **571**, A29 (2014);
Planck Collab. 2015 Results XXVII, Astron. & Astrophys. submitted, arXiv:1502.01598.
78. Planck Collab. 2013 Results XX, Astron. & Astrophys. **571**, A20 (2014);
Planck Collab. 2015 Results XXIV, Astron. & Astrophys. submitted, arXiv:1502.01597.

79. Planck Collab. 2013 Results XXIV, Astron. & Astrophys. **571**, A24 (2014);
Planck Collab. 2015 Results XVII, Astron. & Astrophys. submitted, arXiv:1502.01592.
80. F. Beutler *et al.*, MNRAS **416**, 3017 (2011);
L. Anderson *et al.*, MNRAS **441**, 24 (2014);
E.A. Kazin *et al.*, MNRAS **441**, 3524 (2014);
A.J. Ross *et al.*, MNRAS **449**, 835 (2014).
81. Planck Collab. 2015 Results XIV, Astron. & Astrophys. submitted, arXiv:1502.01590.
82. X. Fan, C.L. Carilli, and B. Keating, Ann. Rev. Astron. Astrophys. **44**, 415 (2006).
83. T.R. Choudhury *et al.*, MNRAS **452**, 261 (2015).
84. M. Kamionkowski and A. Kosowsky, Ann. Rev. Nucl. and Part. Sci. **49**, 77 (1999);
A. Lasenby, Space Sci. Rev. **148**, 329 (2009).
85. Planck Collab. 2015 Results XIX, Astron. & Astrophys. submitted, arXiv:1502.01594.
86. Planck Collab. Interm. Results XXIV, Astron. & Astrophys. **580**, A22 (2015).
87. R. Maartens, Living Rev. Rel. **7**, 7 (2004).